



# Independent Core Rotation in Massive Filaments in Orion

Xuefang Xu (徐雪芳)<sup>1,2</sup>, Di Li (李葳)<sup>1,2,3</sup>, Y. Sophia Dai (戴昱)<sup>4</sup>, Gary A. Fuller<sup>5</sup>, and Nannan Yue (岳楠楠)<sup>1,2</sup>

<sup>1</sup> CAS Key Laboratory of FAST, National Astronomical Observatories, Chinese Academy of Sciences, Beijing 100101, People's Republic of China; [dili@nao.cas.cn](mailto:dili@nao.cas.cn)

<sup>2</sup> University of Chinese Academy of Sciences, Beijing 100049, People's Republic of China

<sup>3</sup> NAOC-UKZN Computational Astrophysics Centre, University of KwaZulu-Natal, Durban 4000, South Africa

<sup>4</sup> Chinese Academy of Sciences South America Center for Astronomy (CASSACA), NAOC, Beijing 100101, People's Republic of China

<sup>5</sup> Jodrell Bank Centre for Astrophysics, Department of Physics and Astronomy, The University of Manchester, Oxford Road, Manchester M13 9PL, UK

Received 2020 January 14; revised 2020 April 14; accepted 2020 April 18; published 2020 May 8

## Abstract

We present high-angular-resolution Atacama Large Millimeter/submillimeter Array images of  $\text{N}_2\text{H}^+$  (1–0) that have been combined with those from the Nobeyama telescope toward the Orion Molecular Cloud (OMC)-2 and OMC-3 filamentary regions. The filaments (with typical widths of  $\sim 0.1$  pc) and dense cores are resolved. The measured 2D velocity gradients of cores are between  $1.3$  and  $16.7$   $\text{km s}^{-1} \text{pc}^{-1}$ , corresponding to a specific angular momentum ( $J/M$ ) between  $0.0012$  and  $0.016$   $\text{pc km s}^{-1}$ . With respect to the core size  $R$ , the specific angular momentum follows a power law  $J/M \propto R^{1.52 \pm 0.14}$ . The ratio ( $\beta$ ) between the rotational energy and gravitational energy ranges from  $0.00041$  to  $0.094$ , indicating insignificant support from rotation against gravitational collapse. We further focus on the alignment between the cores' rotational axes, which is defined to be perpendicular to the direction of the velocity gradient ( $\theta_G$ ), and the direction of elongation of filaments ( $\theta_f$ ) in this massive star-forming region. The distribution of the angle between  $\theta_f$  and  $\theta_G$  was found to be random, i.e., the cores' rotational axes have no discernible correlation with the elongation of their hosting filament. This implies that, in terms of angular momentum, the cores have evolved to be dynamically independent from their natal filaments.

*Unified Astronomy Thesaurus concepts:* [Interstellar medium \(847\)](#); [Interstellar filaments \(842\)](#); [Interstellar clouds \(834\)](#); [Interstellar dynamics \(839\)](#); [Interstellar molecules \(849\)](#)

## 1. Introduction

High spatial and spectral resolution observations that can resolve filaments (with typical widths of  $\sim 0.1$  pc) and cores are powerful tools for studying the dynamic structures of dense gas in massive star formation regions. Herschel images revealed that, in molecular clouds, dense filaments are ubiquitous structures, along which dense cores are commonly found (Molinari et al. 2010; André et al. 2014). Dense cores, presumably the site of current and future star formation, can form within or simultaneously with the filaments (André et al. 2010; Arzoumanian et al. 2011; Chen & Ostriker 2015). Atacama Large Millimeter/submillimeter Array's (ALMA) unprecedented spectral imaging capabilities makes feasible detailed studies of the dynamics of cores and filaments, even in relatively distant massive star-forming regions. In this work, we focus on the angular momentum of cores and its relation with respect to filaments.

For low-mass star-forming regions, earlier studies (e.g., Barranco & Goodman 1998; Caselli et al. 2002; Shinnaga et al. 2004; Puanova et al. 2018) measured the velocity gradients of dense gas at the thermal Jeans scale  $\sim 0.04$  pc, such as in L1495, L1521F, TMC-1C, L1251A, and PER4-7. For massive cores, generally more distant, the typical spatial resolution was  $\sim 0.1$  pc (see, e.g., Pirogov et al. 2003; Li et al. 2012; Tatematsu et al. 2016). With ALMA, we obtained high spatial resolution ( $3''$ ) images of  $\text{N}_2\text{H}^+$  (1–0) toward filaments in OMC-2 and OMC-3. In conjunction with a sufficient velocity resolution of  $0.11$   $\text{km s}^{-1}$ , a sensitive probe into the angular momentum of cores is now feasible down to the  $\sim 0.05$  pc scale, the thermal Jeans scale for these massive star-forming regions.

The Orion Molecular Cloud (OMC), the closest giant molecular cloud with an OB cluster, is an ideal target for

studying the relation between dense cores and filaments. OMC-2 and OMC-3 are relatively quiescent (Li 2002; Li et al. 2003) and filamentary clouds in the OMC. We adopt a distance of 400 pc for OMC-2 and OMC-3 following Nutter & Ward-Thompson (2007). Li et al. (2013a) identified 30 massive quiescent cores, which contain no H II region and no IRAS point sources and are at least 1 pc away from the OB cluster, in OMC-2 and OMC-3. The core kinetic temperatures range from 13 to 31 K. The majority of cores were found to be gravitationally bound and 14 cores to be supercritical, i.e., the observed thermal and nonthermal gas motion cannot prevent immediate collapse (with a reasonable assumption of magnetic field strength  $B \leq 500 \mu$  Gauss).

Widespread and relatively easy to detect,  $\text{N}_2\text{H}^+$  is a reliable tracer of cold ( $T \simeq 10$ – $20$  K), dense ( $n(\text{H}_2) > 10 \times 10^4 \text{ cm}^{-3}$ ) gas (Bergin & Langer 1997; Tafalla et al. 2004, 2006; Crapsi et al. 2005). Benson et al. (1998) found that most (94%) dense cores in their sample had a detectable rotational transition of  $\text{N}_2\text{H}^+$  ( $J = 1$ – $0$ ).  $\text{N}_2\text{H}^+$  is formed through the reaction  $\text{N}_2 + \text{H}^+$  and is mainly destroyed through reaction with CO and electrons (Bergin & Langer 1997; Aikawa et al. 2001; Caselli et al. 2002). Since the abundances of CO and electrons drop in dense gas (Bergin & Langer 1997), the depletion timescale of  $\text{N}_2\text{H}^+$  is longer than many other, particularly carbon-bound, molecules (Bergin & Langer 1997; Aikawa et al. 2001), making  $\text{N}_2\text{H}^+$  (1–0) especially suitable for tracing dense cores and filaments.

To investigate the alignment between the core rotation and the natal filament, we examine the distribution of the angles between the rotational axes and the direction of the filament elongation. Such an angle can potentially discriminate between different mechanisms of core formation. The gravitational fragmentation of a shock-compressed layer (Whitworth et al.

1995), for example, can explain the perpendicular relation between the core angular momentum and filaments. Such a configuration has indeed been found in cores with young-stellar-object-driven outflows (e.g., Anathpindika & Whitworth 2008). In contrast, a near parallel relation can be explained by gravo-turbulent fragmentation (e.g., Banerjee et al. 2006; Offner et al. 2008).

In this Letter, we characterize the orientations of the filaments in OMC-2 and OMC-3 and measure the velocity gradients of 30 cores there based on ALMA  $\text{N}_2\text{H}^+$  (1–0) images. ALMA provided a previously unattainable spatial dynamic range, namely, the size of the longer dimension of dense structures divided by that of the resolution element. The high resolution of ALMA makes measuring velocity gradients of dense gas feasible at the Jeans scale, in young OB-cluster-hosting regions, such as the OMC.

This Letter is organized as follows. Observation and data are described in Section 2. Section 3 presents our measurements of the filament orientation and the velocity gradients. In Section 4, we calculate and analyze the alignment (or lack thereof) between core angular momentum and its natal filament. We also compute the ratio between the rotational energy and gravitational energy. Sections 5 and 6 are the discussion and summary, respectively.

## 2. Data

We mapped OMC-2 and OMC-3 in  $\text{N}_2\text{H}^+$  (1–0) with ALMA in 2014 November and 2015 August in Band 3. The frequency resolution of  $\text{N}_2\text{H}^+$  is 35 kHz, which corresponds to a velocity resolution of  $0.11 \text{ km s}^{-1}$  at 93 GHz. We used the 12 m main array and the Atacama Compact Array (ACA) to mosaic OMC-3 with 11 pointings, and OMC-2 with 7 pointings. The baselines of the 12 m main array and the ACA observations are at a range of 13.6–340.0 m and 6.8–87.4 m, respectively.

The  $\text{N}_2\text{H}^+$  (1–0) images have an angular resolution of  $\sim 3''$ , which allows us to investigate the alignment between the rotation axes (perpendicular to the direction of velocity gradient) of cores and their filaments in OMC-2 and OMC-3. This  $3''$  resolution corresponds to  $\sim 0.06 \text{ pc}$ , smaller than the characteristic scale of filaments and cores (André et al. 2010, 2014; Molinari et al. 2010; Arzoumanian et al. 2011; Chen & Ostriker 2015). This value is comparable to the Jeans scale ( $\sqrt{15k_B T / (4\pi G m \rho)}$ ) of  $\sim 0.05 \text{ pc}$  for gas of  $n \sim 10^6 \text{ cm}^{-3}$  at 15 K, which are typical conditions for the dense filaments and core envelopes in Orion.

The single-dish data of  $\text{N}_2\text{H}^+$  (1–0) were taken from the Nobeyama Radio Observatory Star Formation Legacy Project (Nakamura et al. 2019). The Nobeyama  $\text{N}_2\text{H}^+$  observations were executed with the newly developed 100 GHz Band 4 beam dual-polarization receiver (FOREST) during 2017 January and March. The Nobeyama velocity resolution is  $0.1 \text{ km s}^{-1}$ . The system temperature and noise level are at a range of 150–200 K and 0.26–0.30 K, respectively.

We combined the  $\text{N}_2\text{H}^+$  data from ALMA and Nobeyama to recover missing fluxes in the interferometric data. The combination was performed using Common Astronomy Software Applications (CASA; McMullin et al. 2007). The integrated intensity of the combined  $\text{N}_2\text{H}^+$  (1–0) images and the overlaid cores, labeled 1–30, are shown in Figure 1(a).

## 3. Fitting Filament and Velocity Gradient

### 3.1. Orientations of the Filaments

In this section, we focus on the large-scale filamentary structures ( $\geq 0.3 \text{ pc}$ ) and fit them following the procedures described in Li et al. (2013b). For the  $\text{N}_2\text{H}^+$  integrated density map, the long-axis direction of the autocorrelation function is defined as the filament orientation ( $\theta_f$ ). The fitted filaments in OMC-2 and OMC-3 are shown as the red solid lines in Figure 1(a).

The main steps of fitting filaments to obtain  $\theta_f$  are described as follows. We first apply a two-dimensional Fourier transform to the  $\text{N}_2\text{H}^+$  integrated intensity map, which is then multiplied by its complex conjugate. The inverse transform of the product yields the autocorrelation function. For a given contour of this autocorrelation map, the long-axis direction can be obtained by performing a least-squares fit to the pixel positions located within the contour. The fitting of  $\theta_f$  is robust with respect to the choice of contour levels, as only  $< 5^\circ$  variation was found among different trials. In subsequent calculations, the contour at 20% of the peak value was adopted. Figure 1(b) displays the results from steps above in OMC-3.

### 3.2. Fitting Spectral Lines and Velocity Gradient

Though  $\text{N}_2\text{H}^+$  (1–0) has seven closely spaced hyperfine components, there is an isolated one (the shaded region in Figure 1(c)). For measuring the velocity gradient, we compared fitting all hyperfine components and fitting just the isolated one with a single Gaussian. No significant difference was found. Therefore, we relied on the single-Gaussian fit in all subsequent calculations.

To securely measure the velocity gradient, we require the spectral lines to have peak intensity greater than three times that of the rms noise and fitting errors in the cores. We then fit the velocity field as  $v_{\text{LSR}} = v_0 + a\Delta\alpha + b\Delta\delta$ , and measure the velocity gradients following the method described in Goodman et al. (1993).  $\Delta\alpha$  and  $\Delta\delta$  are the offsets from the center position ( $5^{\text{h}}:35^{\text{m}}:21^{\text{s}}.0$ ,  $-5^\circ:00':00''$ ) of the combined  $\text{N}_2\text{H}^+$  images in the R.A. and decl. in radians, respectively.  $a$  and  $b$  are the projections of the gradient per radian onto the  $\alpha$  and  $\delta$  axes, respectively. The magnitude of the velocity gradient is given by

$$\mathcal{G} = |\nabla v_{\text{LSR}}| = \frac{(a^2 + b^2)^{1/2}}{D}, \quad (1)$$

where  $D$  denotes the distance to the cores. The gradient direction is given by

$$\theta_G = \tan^{-1} \frac{a}{b}. \quad (2)$$

The fitted  $\mathcal{G}$  and  $\theta_G$  are listed in Table 1. The black arrows (Figure 1(a)) with varying length illustrate the velocity gradients.

## 4. Results

In this section, we calculate and analyze the distribution of the angles between filaments and velocity gradients, based on the fitted angular differences  $|\theta_f - \theta_G|$ . We also derive the specific angular momentum  $J/M$  and the ratio  $\beta$  between the rotational energy and gravitational energy, based on the measured velocity gradients.

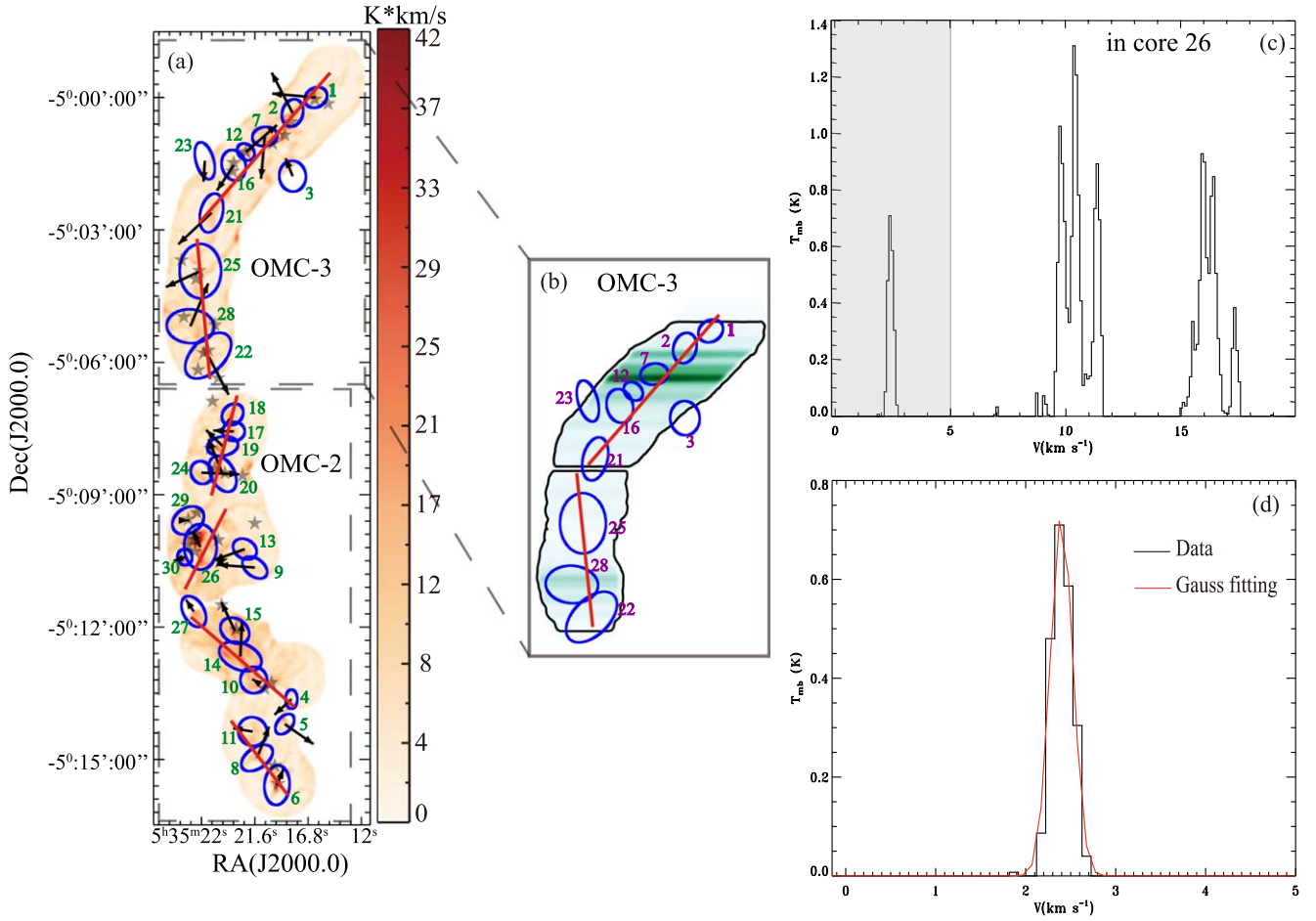


**Figure 1.** (a) Thirty cores overlaid with the integrated intensity of  $\text{N}_2\text{H}^+$  (1–0). The blue ellipses are the size and location of the 30 cores. The black arrows with varying length represent the velocity gradients, as measured in Section 3.2. The lengths of the black arrows are the values of the measured velocity gradients. The red solid lines are the fitted filaments (see Section 3.1). The gray stars are young stellar objects (YSOs). (b) Zoomed-in view of the fitted filaments and their cores in OMC-3. The background is the autocorrelation map of the  $\text{N}_2\text{H}^+$  integrated intensity map. The contour marks 20% of the maximum peak in the autocorrelation map. (c) The brightest  $\text{N}_2\text{H}^+$  peak (in core 26) in OMC-2 and OMC-3. Though  $\text{N}_2\text{H}^+$  (1–0) has hyperfine components, the shaded region refers to a single isolated Gaussian component due to the  $\text{N}_2\text{H}^+$  (1–0) transition. (d) Gaussian fit to the line in the shaded region of (c).

#### 4.1. The Distribution of $|\theta_f - \theta_G|$

To quantify the alignment between the velocity gradients of cores and their filaments,  $|\theta_f - \theta_G|$  is derived as

$$|\theta_f - \theta_G| = \text{MIN}\{|\theta_f - \theta_G|, 180 - |\theta_f - \theta_G|\}, \quad (3)$$

where  $\theta_f$  and  $\theta_G$  are measured clockwise from the east, and “MIN” refers to the minimum angular difference between  $\theta_f$  and  $\theta_G$ . The derived  $|\theta_f - \theta_G|$  values are listed in Table 1 and plotted in Figure 2(a). We find that the gradient directions of seven cores ( $\sim 23\%$ ) are essentially parallel to their filament orientations ( $0^\circ \pm 10^\circ$ ; masked as the dusty blue strip in Figure 2(a)), while the gradient directions of eight cores ( $\sim 27\%$ ) are essentially perpendicular to their filaments ( $90^\circ \pm 10^\circ$ ; the gray strip in Figure 2(a)).

To investigate the distribution of  $|\theta_f - \theta_G|$ , Monte Carlo simulations are performed in three-dimensional (3D) space. We generate two random unit vectors within a unit sphere in 3D, and measure the angle ( $\theta_{3D}$ ) between the two vectors.  $10^6$  pairs of unit vectors are generated to produce  $10^6$  angles of  $\theta_{3D}$ , constrained to a range of  $0^\circ$ – $90^\circ$ . If  $\theta_{3D}$  is larger than  $90^\circ$ , the  $180^\circ - \theta_{3D}$  values are adopted (Equation (3)). For  $\theta_{3D}$  in the range of  $0^\circ$ – $20^\circ$ , we define it as parallel, while  $20^\circ$ – $70^\circ$  is defined as random, and  $70^\circ$ – $90^\circ$  as perpendicular. Then we

project the angles of  $\theta_{3D}$  onto a two-dimensional (2D) space. Figure 2(b) plots the cumulative distribution function of our  $|\theta_f - \theta_G|$  and the projected  $\theta_{3D}$ . The details of the Monte Carlo simulations can be found in Appendix A of Stephens et al. (2017). The  $p$ -values of the Anderson–Darling (AD) test are used to indicate whether two distributions are consistent.  $p$ -values near 1 imply that the two distributions are likely consistent, while  $p$ -values near 0 imply that they are not consistent. For the distribution of our  $|\theta_f - \theta_G|$  and the simulated random distribution, the AD test gives a  $p$ -value of 0.97, consistent with being random. This result indicates no correlation between the gradient direction of a core and its filament orientation. This is consistent with the scenario that the rotation axis of a core is independent of the orientation of the large-scale filament in which it resides.

#### 4.2. $J/M$ and $\beta$ Calculations

The  $J/M$  and  $\beta$  calculations were performed under the assumption that cores have a power-law profile density ( $\rho \propto R^{-1.6}$ ; Bonnor 1956). We used the following equations to calculate  $J/M$  and  $\beta$ :

$$J/M = 0.059GR^2, \quad (4)$$

**Table 1**  
Dynamic Parameters of Orion Cores

Core	R.A. (J2000)	Decl. (J2000)	Mass ( $M_{\odot}$ )	Mass <sub>vir</sub> ( $M_{\odot}$ )	Major "	Minor "	Major Axis Orientation (deg E of N)	$\mathcal{G}$ ( $\text{km s}^{-1} \text{pc}^{-1}$ )	$\theta_G$ (deg E of N)	$J/M$ ( $\text{pc km s}^{-1}$ )	$\beta$	$ \theta_f - \theta_G $ (deg)
1	5:35:16.1	-5:00:00	12.4	6.6	16.0	13.0	3	$2.2 \pm 0.3$	$47 \pm 6$	$1.2 \times 10^{-3} \pm 1.7 \times 10^{-4}$	$1.7 \times 10^{-3} \pm 3.3 \times 10^{-5}$	$81 \pm 12$
2	5:35:18.2	-5:00:21	25.9	5.2	19.0	14.0	12	$1.6 \pm 0.3$	$59 \pm 8$	$1.9 \times 10^{-3} \pm 1.8 \times 10^{-4}$	$1.8 \times 10^{-3} \pm 1.5 \times 10^{-5}$	$38 \pm 16$
3	5:35:18.2	-5:01:47	3.1	3.0	21.0	18.0	52	$10.3 \pm 2.6$	$29 \pm 9$	$9.5 \times 10^{-3} \pm 1.6 \times 10^{-3}$	$3.2 \times 10^{-2} \pm 8.7 \times 10^{-4}$	$63 \pm 6$
4	5:35:18.3	-5:13:38	0.3	0.4	13.0	8.0	35	$9.1 \pm 1.1$	$-86 \pm 3$	$3.8 \times 10^{-3} \pm 2.2 \times 10^{-4}$	$7.8 \times 10^{-2} \pm 2.8 \times 10^{-4}$	$79 \pm 12$
5	5:35:18.9	-5:14:12	0.5	1.2	16.0	10.0	55	$5.1 \pm 0.8$	$35 \pm 6$	$1.9 \times 10^{-3} \pm 2.8 \times 10^{-4}$	$1.1 \times 10^{-2} \pm 2.5 \times 10^{-4}$	$22 \pm 3$
6	5:35:19.6	-5:15:35	5.8	5.7	27.0	17.0	3	$11.1 \pm 0.3$	$139 \pm 1$	$1.1 \times 10^{-2} \pm 2.7 \times 10^{-4}$	$1.8 \times 10^{-2} \pm 1.1 \times 10^{-5}$	$54 \pm 19$
7	5:35:20.7	-5:00:53	30.0	1.8	17.0	13.0	14	$2.6 \pm 0.2$	$-14 \pm 3$	$1.3 \times 10^{-3} \pm 1.3 \times 10^{-4}$	$8.0 \times 10^{-4} \pm 8.0 \times 10^{-6}$	$19 \pm 22$
8	5:35:21.4	-5:14:58	4.0	2.1	24.0	14.0	26	$5.6 \pm 0.3$	$124 \pm 2$	$3.4 \times 10^{-3} \pm 2.3 \times 10^{-4}$	$2.9 \times 10^{-2} \pm 1.3 \times 10^{-4}$	$69 \pm 6$
9	5:35:21.6	-5:10:39	1.6	1.4	19.0	12.0	47	$4.7 \pm 0.4$	$3 \pm 3$	$1.7 \times 10^{-3} \pm 2.1 \times 10^{-4}$	$2.4 \times 10^{-2} \pm 3.6 \times 10^{-4}$	$6 \pm 9$
10	5:35:21.7	-5:13:12	9.2	6.8	18.0	18.0	19	$16.2 \pm 0.4$	$70 \pm 1$	$8.3 \times 10^{-3} \pm 2.6 \times 10^{-4}$	$9.5 \times 10^{-2} \pm 9.4 \times 10^{-5}$	$55 \pm 8$
11	5:35:21.8	-5:14:22	5.7	4.0	20.0	19.0	55	$10.2 \pm 0.2$	$82 \pm 1$	$8.5 \times 10^{-3} \pm 1.9 \times 10^{-4}$	$1.4 \times 10^{-2} \pm 7.6 \times 10^{-5}$	$69 \pm 22$
12	5:35:22.4	-5:01:14	15.6	1.2	13.0	10.0	1	$3.1 \pm 0.7$	$136 \pm 9$	$6.0 \times 10^{-4} \pm 2.0 \times 10^{-4}$	$4.1 \times 10^{-4} \pm 4.6 \times 10^{-5}$	$11 \pm 16$
13	5:35:22.5	-5:10:14	2.5	5.4	17.0	13.0	37	$5.9 \pm 0.3$	$-15 \pm 2$	$3.2 \times 10^{-3} \pm 5.8 \times 10^{-5}$	$1.1 \times 10^{-2} \pm 3.6 \times 10^{-5}$	$12 \pm 10$
14	5:35:22.9	-5:12:40	26.3	6.7	30.0	18.0	37	$5.2 \pm 0.4$	$121 \pm 3$	$9.3 \times 10^{-3} \pm 3.4 \times 10^{-4}$	$2.6 \times 10^{-2} \pm 3.5 \times 10^{-5}$	$74 \pm 21$
15	5:35:23.4	-5:12:05	12.8	3.2	21.0	16.0	2	$6.2 \pm 0.6$	$61 \pm 4$	$2.6 \times 10^{-3} \pm 3.1 \times 10^{-4}$	$5.8 \times 10^{-3} \pm 8.3 \times 10^{-5}$	$46 \pm 5$
16	5:35:23.5	-5:01:32	23.1	5.7	21.0	16.0	3	$6.6 \pm 0.4$	$-24 \pm 2$	$4.0 \times 10^{-3} \pm 2.5 \times 10^{-4}$	$7.6 \times 10^{-3} \pm 2.9 \times 10^{-5}$	$9 \pm 13$
17	5:35:23.5	-5:07:34	7.6	3.0	15.0	13.0	39	$10.0 \pm 0.5$	$28 \pm 2$	$4.6 \times 10^{-3} \pm 2.2 \times 10^{-4}$	$4.2 \times 10^{-2} \pm 9.2 \times 10^{-5}$	$42 \pm 20$
18	5:35:23.6	-5:07:11	6.1	3.4	16.0	13.0	32	$16.6 \pm 0.5$	$-55 \pm 1$	$8.5 \times 10^{-3} \pm 2.3 \times 10^{-4}$	$1.7 \times 10^{-2} \pm 1.2 \times 10^{-4}$	$9 \pm 4$
19	5:35:24.5	-5:07:54	11.7	3.1	21.0	13.0	17	$9.1 \pm 0.5$	$70 \pm 3$	$6.0 \times 10^{-3} \pm 3.2 \times 10^{-4}$	$3.5 \times 10^{-2} \pm 9.7 \times 10^{-5}$	$84 \pm 2$
20	5:35:24.5	-5:08:32	9.7	3.7	26.0	16.0	3	$4.2 \pm 0.2$	$80 \pm 2$	$2.4 \times 10^{-3} \pm 1.9 \times 10^{-4}$	$5.7 \times 10^{-3} \pm 3.6 \times 10^{-5}$	$86 \pm 7$
21	5:35:25.5	-5:02:37	6.8	3.5	27.0	15.0	63	$1.6 \pm 0.2$	$-10 \pm 4$	$1.7 \times 10^{-3} \pm 2.1 \times 10^{-4}$	$4.0 \times 10^{-3} \pm 5.9 \times 10^{-5}$	$23 \pm 11$
22	5:35:25.8	-5:05:51	13.0	4.3	38.0	22.0	7	$2.0 \pm 0.1$	$-118 \pm 3$	$5.5 \times 10^{-3} \pm 2.1 \times 10^{-4}$	$1.5 \times 10^{-2} \pm 2.1 \times 10^{-5}$	$66 \pm 6$
23	5:35:26.1	-5:01:26	3.8	0.7	26.0	12.0	39	$9.8 \pm 1.0$	$-71 \pm 5$	$8.8 \times 10^{-3} \pm 5.1 \times 10^{-4}$	$1.8 \times 10^{-2} \pm 7.0 \times 10^{-4}$	$37 \pm 10$
24	5:35:26.4	-5:08:30	3.8	5.9	16.0	14.0	19	$4.4 \pm 0.6$	$-107 \pm 7$	$2.9 \times 10^{-3} \pm 2.8 \times 10^{-4}$	$3.2 \times 10^{-2} \pm 2.9 \times 10^{-4}$	$87 \pm 7$
25	5:35:26.5	-5:03:56	13.2	12.8	37.0	28.0	2	$4.1 \pm 0.1$	$-70 \pm 1$	$6.8 \times 10^{-3} \pm 2.0 \times 10^{-4}$	$2.1 \times 10^{-2} \pm 1.9 \times 10^{-5}$	$55 \pm 4$
26	5:35:26.5	-5:10:11	33.5	8.3	31.0	22.0	10	$10.8 \pm 0.2$	$14 \pm 1$	$1.6 \times 10^{-2} \pm 2.8 \times 10^{-4}$	$5.8 \times 10^{-2} \pm 1.8 \times 10^{-5}$	$17 \pm 15$
27	5:35:27.1	-5:11:39	2.3	4.5	23.0	14.0	38	$11.9 \pm 0.7$	$37 \pm 2$	$2.5 \times 10^{-3} \pm 5.1 \times 10^{-4}$	$2.7 \times 10^{-2} \pm 1.2 \times 10^{-5}$	$22 \pm 7$
28	5:35:27.4	-5:05:11	20.1	3.2	32.0	23.0	16	$1.3 \pm 0.1$	$108 \pm 3$	$2.5 \times 10^{-3} \pm 1.5 \times 10^{-4}$	$2.2 \times 10^{-4} \pm 8.1 \times 10^{-6}$	$79 \pm 4$
29	5:35:27.6	-5:09:35	12.9	12.8	23.0	17.0	1	$16.7 \pm 0.5$	$95 \pm 1$	$9.9 \times 10^{-3} \pm 3.6 \times 10^{-4}$	$7.6 \times 10^{-2} \pm 1.0 \times 10^{-4}$	$41 \pm 21$
30	5:35:27.9	-5:10:25	6.4	3.3	11.0	10.0	16	$12.8 \pm 1.1$	$-41 \pm 4$	$3.9 \times 10^{-3} \pm 2.4 \times 10^{-4}$	$5.0 \times 10^{-3} \pm 1.8 \times 10^{-4}$	$38 \pm 8$

**Note.** The values of Mass and Mass<sub>vir</sub> are from Li et al. (2013a). Major and Minor axes are from Nutter & Ward-Thompson (2007). Major axis orientation is the major axis direction of cores.

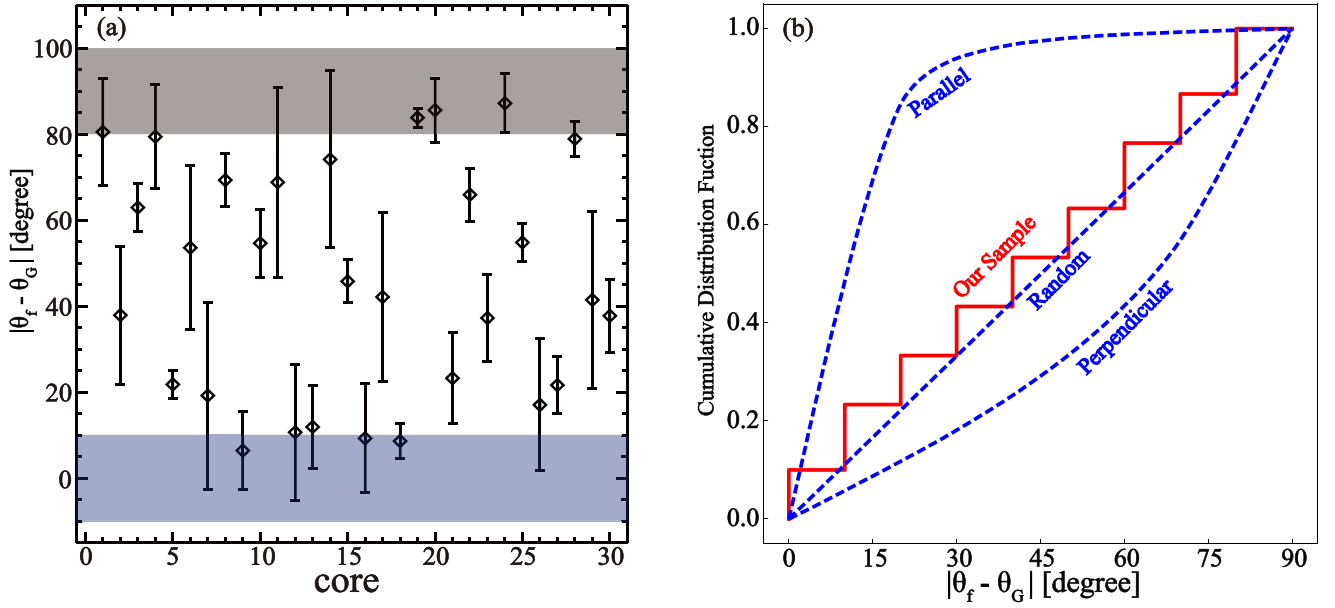


**Figure 2.** (a)  $|\theta_f - \theta_G|$  for each of the 30 cores. The gray strip corresponds to the perpendicular directions, i.e.,  $90^\circ \pm 10^\circ$ . The dusty blue strip corresponds to the parallel directions, i.e.,  $0^\circ \pm 10^\circ$ . (b) The cumulative distribution function of  $|\theta_f - \theta_G|$  and the projected  $\theta_{3D}$ . The red step line is the  $|\theta_f - \theta_G|$  of our sample. The three blue dashed lines are results from the Monte Carlo simulation.

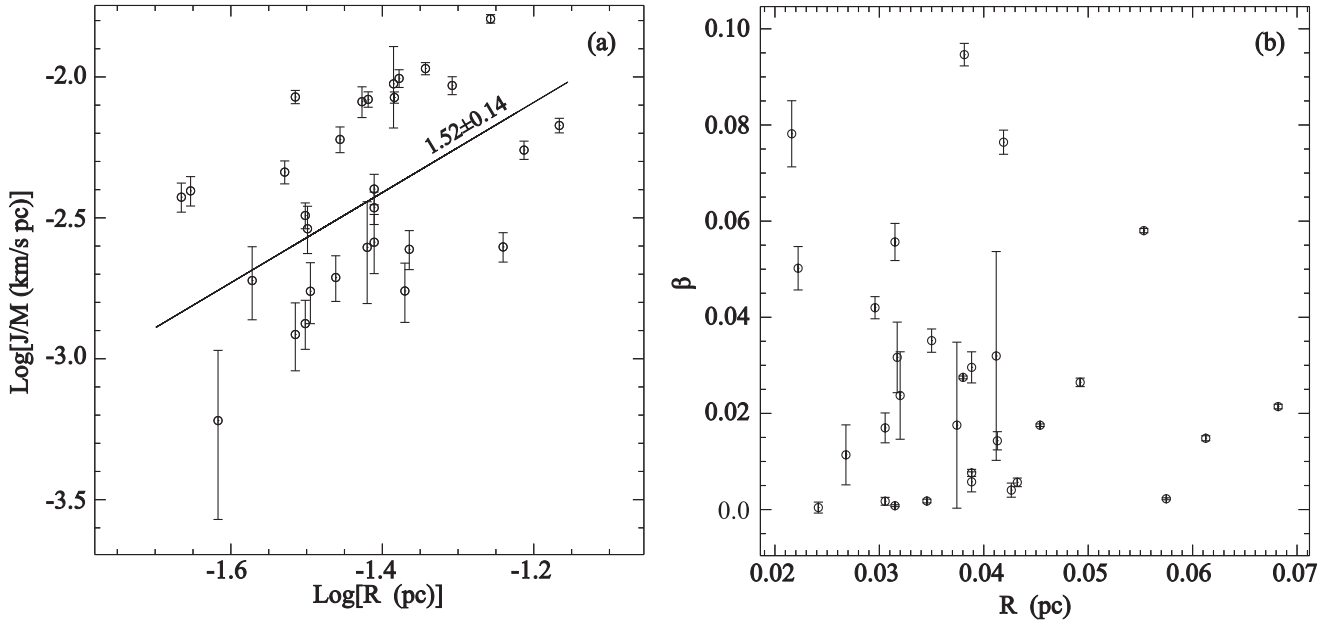


**Figure 3.** The correlation between core size  $R$  and (a) specific angular momentum  $J/M$  and (b)  $\beta$ : ratio between rotational and gravitational energy. The best-fit power-law relation between  $J/M$  and  $R$  as well as corresponding coefficients are labeled in (a).

and

$$\beta = \frac{0.34G^2R^3}{GM}. \quad (5)$$

$M$  is the mass within a radius  $R$ . The calculated  $J/M$  and  $\beta$  are listed in Table 1, and plotted in Figures 3(a) and (b), respectively. We find that  $J/M$  increases with increasing  $R$ , following a power law  $J/M \propto R^{1.52 \pm 0.14}$ . The slope is consistent with the index value of 1.6 found by Goodman et al. (1993) for a sample of dark clouds.  $\beta$  ranges from 0.00041 to 0.094, with no significant correlation with  $R$ . As investigated in previous studies (Goldsmith & Arquilla 1985;

Goodman et al. 1993; Caselli et al. 2002; Curtis & Richer 2011; Tatematsu et al. 2016), these small values of  $\beta$  indicate that rotation alone is not enough to support the core from collapsing due to gravity.

## 5. Discussion

Magnetic fields play an important role during the collapse and fragmentation of massive molecular clumps, as well as the formation of dense cores. Zhang et al. (2014) found that the magnetic fields at dense core scales are either aligned with or perpendicular to the parsec-scale magnetic fields. One may reasonably expect such bimodality for the angles between core

rotation and filament elongation. Anathpindika & Whitworth (2008) reported that the rotational axes of prestellar cores are perpendicular to their filaments. Stephens et al. (2017) showed that a mix of parallel and perpendicular angles exist between the rotation axes of protostellar cores and their filaments. In our sample, however, we find no correlation between the rotational direction and the natal filament's elongation. The distribution is found to be consistent with being random. Similar results were also seen in earlier observations (e.g., Heyer 1988; Davis et al. 2009; Lee et al. 2016; Offner et al. 2016; Puanova et al. 2018).

Considerable differences exist among the analyses mentioned above, in terms of sample sizes, definition of filament and cores, and the fitting of rotation and elongation. Anathpindika & Whitworth (2008) and Stephens et al. (2017) regarded the outflow orientations as the rotation axes of prestellar/protostellar cores, while the directions of velocity gradients trace the rotation axes of cores in Puanova et al. (2018), as well as in our sample. Stephens et al. (2017) identified filaments using FILFINDER (Koch & Rosolowsky 2015) and SExtractor (Bertin & Arnouts 1996), while some studies (Arzoumanian et al. 2018; Bresnahan et al. 2018; Gong et al. 2018; Tanimura et al. 2019) employed DisPerSE (Sousbie 2011) to trace filaments. Although our experience seems to suggest that these technical differences are unlikely to explain the diversity in the relative orientations between rotation and filament, high spectral and spatial images of a much larger sample are needed to tackle the issue systematically.

## 6. Summary

We mapped  $N_2H^+$  (1–0) in OMC-2 and OMC-3 with both ALMA and Nobeyama at 93 GHz. The combined single-dish and interferometric data offer a rare opportunity to study the relative orientation between the rotational axes of the massive quiescent cores and the elongation of their natal filaments, down to the thermal Jeans scale of dense gas in a massive star-forming region. Our results are summarized as follows.

1. The angle ( $|\theta_f - \theta_G|$ ) between the orientation of the filaments ( $\theta_f$ ) and the direction of core velocity gradient  $\theta_f$  was found to be random, based on a Monte Carlo simulation. The core rotation seems to have disengaged itself from its natal filament and, by association, the large-scale magnetic field.

2. The measured velocity gradients of 30 cores range from 1.3 to 16.7  $\text{km s}^{-1} \text{pc}^{-1}$ . The measured specific angular momentum ( $J/M$ ) ranges from 0.0012 to 0.016  $\text{pc km s}^{-1}$ . A power-law scaling was found between the specific angular momentum and the core size as  $J/M \propto R^{1.52 \pm 0.14}$ .

3. The ratio  $\beta$  between the rotational and gravitational energy ranges from 0.00041 to 0.094, indicating that rotation cannot stop gravitational collapse in these dense cores.

This work is supported by the National Natural Science Foundation of China grant No. 11988101, No. 11725313, No. 11721303 and the International Partnership Program of Chinese Academy of Sciences grant No. 114A11KYSB20160008. This Letter makes use of the following ALMA data: ADS/JAO.ALMA#2013.1.00662.S. ALMA is a partnership of ESO (representing its member states), NSF (USA) and NINS (Japan), together with NRC

(Canada), MOST and ASIAA (Taiwan), and KASI (Republic of Korea), in cooperation with the Republic of Chile. The Joint ALMA Observatory is operated by ESO, AUI/NRAO and NAOJ.

## ORCID iDs

Xuefang Xu

(徐雪芳)  <https://orcid.org/0000-0001-8514-6989>

Di Li (李韵)  <https://orcid.org/0000-0003-3010-7661>

Y. Sophia Dai

(戴昱)  <https://orcid.org/0000-0002-7928-416X>

Gary A. Fuller  <https://orcid.org/0000-0001-8509-1818>

Nannan Yue

(岳楠楠)  <https://orcid.org/0000-0003-0355-6875>

## References

- Aikawa, Y., Ohashi, N., Inutsuka, S.-I., et al. 2001, *ApJ*, 552, 639
- Anathpindika, S., & Whitworth, A. P. 2008, *A&A*, 487, 605
- André, P., di Francesco, J., Ward-Thompson, D., et al. 2014, in *Protostars and Planets VI*, ed. H. Beuther et al., Vol. 27 (Tucson, AZ: Univ. Arizona Press), 27
- André, P., Men'shchikov, A., Bontemps, S., et al. 2010, *A&A*, 518, L102
- Arzoumanian, D., André, P., Didelon, P., et al. 2011, *A&A*, 529, L6
- Arzoumanian, D., Shimajiri, Y., Inutsuka, S.-I., et al. 2018, *PASJ*, 70, 96
- Banerjee, R., Pudritz, R. E., & Anderson, D. W. 2006, *MNRAS*, 373, 1091
- Barranco, J. A., & Goodman, A. A. 1998, *ApJ*, 504, 207
- Benson, P. J., Caselli, P., & Myers, P. C. 1998, *ApJ*, 506, 743
- Bergin, E. A., & Langer, W. D. 1997, *ApJ*, 486, 316
- Bertin, E., & Arnouts, S. 1996, *A&AS*, 117, 393
- Bonnor, W. B. 1956, *MNRAS*, 116, 351
- Bresnahan, D., Ward-Thompson, D., Kirk, J. M., et al. 2018, *A&A*, 615, A125
- Caselli, P., Benson, P. J., Myers, P. C., et al. 2002, *ApJ*, 572, 238
- Chen, C.-Y., & Ostriker, E. C. 2015, *ApJ*, 810, 126
- Crapsi, A., Caselli, P., Walmsley, C. M., et al. 2005, *ApJ*, 619, 379
- Curtis, E. I., & Richer, J. S. 2011, *MNRAS*, 410, 75
- Davis, C. J., Froebrich, D., Stanke, T., et al. 2009, *A&A*, 496, 153
- Goldsmith, P. F., & Arquilla, R. 1985, in *Protostars and Planets II*, ed. D. C. Black & M. S. Matthews (Tucson, AZ: Univ. Arizona Press), 137
- Gong, Y., Li, G. X., Mao, R. Q., et al. 2018, *A&A*, 620, A62
- Goodman, A. A., Benson, P. J., Fuller, G. A., et al. 1993, *ApJ*, 406, 528
- Heyer, M. H. 1988, *ApJ*, 324, 311
- Koch, E. W., & Rosolowsky, E. W. 2015, *MNRAS*, 452, 3435
- Lee, K. I., Dunham, M. M., Myers, P. C., et al. 2016, *ApJL*, 820, L2
- Li, D. 2002, PhD thesis, Cornell Univ.
- Li, D., Goldsmith, P. F., & Menten, K. 2003, *ApJ*, 587, 262
- Li, D., Kauffmann, J., Zhang, Q., et al. 2013a, *ApJL*, 768, L5
- Li, H.-B., Fang, M., Henning, T., et al. 2013b, *MNRAS*, 436, 3707
- Li, J., Wang, J., Gu, Q., et al. 2012, *ApJ*, 745, 47
- McMullin, J. P., Waters, B., Schiebel, D., et al. 2007, in *ASP Conf. Ser.* 376, *Astronomical Data Analysis Software and Systems XVI*, ed. R. A. Shaw, F. Hill, & D. J. Bell (San Francisco, CA: ASP), 127
- Molinari, S., Swinyard, B., Bally, J., et al. 2010, *A&A*, 518, L100
- Nakamura, F., Ishii, S., Dobashi, K., et al. 2019, arXiv:1909.05980
- Nutter, D., & Ward-Thompson, D. 2007, *MNRAS*, 374, 1413
- Offner, S. S. R., Dunham, M. M., Lee, K. I., et al. 2016, *ApJL*, 827, L11
- Offner, S. S. R., Klein, R. I., & McKee, C. F. 2008, *ApJ*, 686, 1174
- Pirogov, L., Zinchenko, I., Caselli, P., et al. 2003, *A&A*, 405, 639
- Puanova, A., Caselli, P., Pineda, J. E., et al. 2018, *A&A*, 617, A27
- Shinnaga, H., Ohashi, N., Lee, S.-W., et al. 2004, *ApJ*, 601, 962
- Sousbie, T. 2011, *MNRAS*, 414, 350
- Stephens, I. W., Dunham, M. M., Myers, P. C., et al. 2017, *ApJ*, 846, 16
- Tafalla, M., Myers, P. C., Caselli, P., et al. 2004, *A&A*, 416, 191
- Tafalla, M., Santiago-García, J., Myers, P. C., et al. 2006, *A&A*, 455, 577
- Tanimura, H., Aghanim, N., Bonjean, V., et al. 2019, arXiv:1911.09706
- Tatematsu, K., Ohashi, S., Sanhueza, P., et al. 2016, *PASJ*, 68, 24
- Whitworth, A. P., Chapman, S. J., Bhattal, A. S., et al. 1995, *MNRAS*, 277, 727
- Zhang, Q., Qiu, K., Girart, J. M., et al. 2014, *ApJ*, 792, 116